Lab on a Chip

PAPER

View Article Online
View Journal

Cite this: DOI: 10.1039/d5lc00162e

A multi-channel wearable sensing patch based on gate-all-around field-effect transistors†

Zhe Xing, ‡[ab] Qiang Liu,‡[bc] Bo Lin, [ab] Shuang Li,[d] Yuxin Liu,[bc] Guanyang Zhang,[bc] Wenjie Yu,[bc] Zhenhua Wu*[ab] and Hongju Mao*[abe]

Received 18th February 2025,
Accepted 19th May 2025

DOI: 10.1039/d5lc00162e

rsc.li/loc

Field-effect transistors (FETs), known for their rapid response and signal amplification capabilities, have attracted significant research interest for the detection of biomarkers. However, the development of multi-channel sensors using FETs and their wearable applications are impeded by the rigid substrates and large areas. Here, we reported a wearable EGFET sensor array patch that integrates gate-all-around field-effect transistors (GAA FETs) and flexible printed circuit board (FPCB) patches to overcome these challenges. The patch takes advantage of the excellent electrical properties and small size of GAA FETs, allowing for multi-biomarker detection. Additionally, it integrates large-scale, low-cost FPCB-based electrodes to enhance the flexibility of the patch. Comprehensive characterization experiments have demonstrated the performance of the patch to detect multiple biomarkers, including glucose, lactate, Na^+, K^+, and Ca^{2+}. This innovative patch is promising to facilitate the development of FET-based multi-channel wearable sensors, and has the potential to help realize more comprehensive health monitoring.

Introduction

Sweat contains a large number of health-related chemicals, which has attracted significant attention from researchers.[1–4] Compared to blood analysis, which usually requires invasive methods, sweat has the advantage that it can be easily and non-invasively collected from various parts of the body.[5] As a result, sweat has become an ideal biofluid for wearable sensors.

Wearable sweat sensing platforms eliminate the reliance on traditional face-to-face visits and costly clinical tests, thereby significantly improving the efficiency of diagnosis and assessment.[6] Furthermore, measuring individual biomarkers does not meet the need for comprehensive health monitoring. Assessing health conditions, predicting and evaluating pathological or physiological abnormalities requires the measurement of multiple biomarkers (*e.g.*, lactate, glucose, Na^+, K^+, and Ca^{2+}, among others). In particular, sodium (Na^+) and potassium (K^+) play a crucial role in maintaining electrolyte balance and preventing hypertension,[7] while calcium (Ca^{2+}) levels correlate with bone disease and thyroid dysfunction.[8,9] Lactate level can be used as a reference to regulate the intensity of exercise,[10] while blood glucose level is an indicator that diabetics need to pay attention to.[11,12] The concentrations of the above components in sweat are thought to have some relationship with their concentrations in the blood.[13,14] To enable multi-biomarker measurements, multimodal biochemical sensors have been proposed that integrate individual biomarker sensors into arrays for comprehensive health monitoring.

Field-effect transistors (FETs) have unique features, such as the ability for array integration and compatibility with integrated circuits, which make them very promising for multimodal and multichannel sensors. Numerous studies have been conducted to modify the channel between the source and drain so that the charge density of the semiconductor channel can be altered by recognizing the target analyte.[15–19] This specific recognition affects the electrical response of the FET, allowing for fast and label-free monitoring. Extended gate field-effect transistors (EGFETs) are another type of FET sensing structure. In this structure there is no modification of the FET channel, but rather the FET gate is connected to an external sensing electrode (extended gate, EG) *via* a wire.[20] Similar to normal FET

[a] State Key Laboratory of Transducer Technology, Shanghai Institute of Microsystem and Information Technology, Chinese Academy of Sciences, Shanghai, 200050, China. E-mail: wuzhx@mail.sim.ac.cn, hongjumao2002@126.com
[b] Center of Materials Science and Optoelectronics Engineering, University of Chinese Academy of Sciences, Beijing, 100049, China
[c] National Key Laboratory of Materials for Integrated Circuits, Shanghai Institute of Microsystem and Information Technology, Chinese Academy of Sciences, Shanghai, 200050, China
[d] Academy of Medical Engineering and Translational Medicine, Tianjin University, Tianjin, 300072, China
[e] Center for Medical Research and Innovation, Shanghai Pudong Hospital, Fudan University Pudong Medical Center, Shanghai, 200120, China

† Electronic supplementary information (ESI) available: Design and fabrication method of the FPCB patch, detailed characterization of GAA FETs and the FPCB patch, evaluation of the output current and the selectivity of EGFET sensing patch, the current response in the subthreshold region. See DOI: https://doi.org/10.1039/d5lc00162e

‡ These authors contributed equally to this paper.

sensors, the EGFET also has advantages including fast response, high sensitivity and front-end signal amplification. In addition, another FET sensor called an ISFET has similar structure to the EGFET, but it requires a complex packaging scheme to avoid channel pollution. In contrast, the EGFET isolates the solution from the FET channel, thereby reducing solution-induced instabilities such as signal drift and dissolution or leakage of the channel material.[21] Furthermore, the simple structure of the EGFET allows for direct signal output, making it a promising approach for point-of-care (POCT) applications.[22–24] Since the advantages of EGFETs are well suited for system miniaturization, many studies have developed EGFET-based handheld devices or miniature instruments. By connecting EGs with different functions, sensing of specific target analytes can be achieved, avoiding the modification of the FET channel. Chen *et al.*[25] constructed a portable wireless sensing platform using commercial metal-oxide-semiconductor field-effect transistors (MOSFETs) and graphene EGs for the ultrasensitive detection of urinary cystatin C to provide early screening for chronic kidney disease. Kuppuswamy *et al.*[26] developed an EGFET based on NiO_X template-grown Ni-MOF-Coated carbon paper electrodes. Ho *et al.*[27] designed an ITO based EGFET biosensor and used immobilized single-stranded DNA (ssDNA) to detect hepatitis C virus (HCV)-viral RNA. These advances demonstrated that EGFETs can transduce and amplify sensing signals for a variety of target analytes. Apart from conventional MOSFETs, there have also been research efforts to realize EGFETs by designing special structures. Shi *et al.*[28] reported an EGFET gas sensor based on semiconductor single-walled carbon nanotubes to address the compatibility issue between gas-sensitive elements and CMOS technology. Regarding wearable applications of EGFETs, Zheng *et al.*[29] combined commercial MOSFETs to design a microneedle-based wearable EGFET platform, while Mano *et al.*[30] developed a flexible EGFET sensor based on organic transistors for glucose detection. Richardson *et al.*[31] demonstrated a low-power biochemical sensing platform using extended gate field-effect transistors (EGFET) to monitor neuropeptide Y (NPY) in sweat in a range of 100 fM to 100 nM. Moreover, Shen *et al.*[32] developed an active-matrix extended-gate field-effect transistor (AMEGFET) array that can perform instant analysis of various metabolites. This design simplifies the readout circuitry and avoids the mutual interferences. Here, Sheibani *et al.*[33] reported a wearable sensory electronic chip based on a platinum/graphene aptamer extended gate field effect transistor (EG-FET) for the recognition of cortisol in biological buffers within the Debye screening length. These studies demonstrate the feasibility of EGFETs in building wearable sensors.

Although the application of EGFETs is rapidly advancing, most research still focuses on detecting single target analytes. This limitation arises because the FETs used are often commercially packaged MOSFETs or fabricated with new processes, which typically have large areas.[24,34–36] These large-area FETs are not suitable for forming sensor arrays, thus hindering the development of multi-channel sensing platforms. This limitation also impedes the application of EGFETs in wearable devices, as the large size restricts the placement to larger, flatter body areas (such as the chest, abdomen, and back) and reduces wearing comfort. Moreover, the rigid substrates of MOSFETs and other devices manufactured through CMOS processes also limits the use of EGFETs on the skin surface.

Herein, we developed a flexible EGFET sensor array that combines FPCB patches and Gate-all-around field-effect transistors (GAA FETs). This EGFET sensor array is capable of detecting sweat constituents including glucose, lactate, Na, K, and Ca, making it suitable for wearable sweat monitoring applications. The gate-all-around field-effect transistor (GAA FET) is a novel type of FET, where the gate completely surrounds the semiconductor channel, providing exceptional control over the channel's electric field.[37,38] This special gate structure results in higher transconductance, lower driving voltage, and greater electron mobility, which theoretically enhances the sensing signals of EGFETs. In addition, the GAAFETs have very small subthreshold swings, which means that the drain current is more sensitive to changes in gate voltage. The GAA FET devices used in this study are fairly small, with approximately 36 devices fitting within an area of about 2.9 mm × 1.4 mm. Therefore, the composition of sensor arrays does not lead to excessive area. Consequently, the number of sensing channels is only limited by the size of the EGs. The sensing electrode array is fabricated using FPCB technology and is connected to the GAA FETs placed on the FPCB patches. This setup effectively isolates the GAA FETs from the solution and forms a comprehensive flexible EGFET. When the sensing electrodes interact with the target analytes in sweat, the gate potential of the GAA FETs is affected, thereby changing the threshold voltage and current response. Consequently, this allows for the quantitative analysis of the target analytes. This study demonstrates the intrinsic properties of GAA FETs, the sensing performance of enzyme and ion sensors, and the capability of the patch to monitor sweat.

In brief, this work innovatively combines GAA FETs and FPCB electrodes to construct a EGFET multi-channel flexible sensing patch, providing a novel methodology for developing large-scale array-based wearable sensors. This patch takes advantage of GAAFET's fast response, signal amplification and sub-threshold regime to produce a highly sensitive sensor. Theoretically, this patch can be expanded to detect a lot more than five target analytes. Additionally, the FPCB-based array is suitable for integration with miniature circuit systems. From a future perspective, this work demonstrates the significant potential of the EGFET multi-channel flexible sensing platform for wearable applications.

Experimental section

Materials and reagents

Selectophore grade sodium ionophore X, calcium ionophore II (ETH 129), sodium tetrakis[3,5-bis(trifluoromethyl)phenyl]

borate (Na-TFPB), bis(2-ethylehexyl) sebacate (DOS), high-molecular-weight poly(vinyl chloride) (PVC), polyvinyl butyral (PVB), tetrahydrofuran (THF), valinomycin (potassium ionophore), gold(III) chloride trihydrate, iron(III) chloride(FeCl3), potassium ferricya-nide(III) [$K_3Fe(CN)_6$], chitosan, multi-walled carbon nanotube, nickel(II) nitrate hexahydrate ($Ni(NO_3)_2{\cdot}6H_2O$), D-(+)-glucose, L-(+)-lactic acid, uric acid (UA), bovine serum albumin (BSA), nafion (5% wt), glucose oxidase, ethylene glycol (EG), were obtained from Sigma Aldrich (USA). L-lactate oxidase (>80 activity units per milligram) was procured from Toyobo Crop. (Japan). Sodium chloride (NaCl), calcium chloride ($CaCl_2$), potassium chloride (KCl), magnesium chloride ($MgCl_2$) and phosphate buffered saline (PBS) were obtained from Sangon Biotech Co. Ltd. (Shanghai, China). Sulfuric acid (H_2SO_4), hydrochloric acid (HCl), and ammonium chloride (NH_4Cl) were obtained from Shanghai Lingfeng Chemical Reagent Co. Ltd. (Shanghai, China). Carbon inks and Ag/AgCl inks were obtained from Engineered Materials Systems, Inc. (EMS). Sodium tetraphenylborate (Na-TPB) was obtained from Aladdin. Creatinine and ascorbic acid (AA) were obtained from Adamas-beta. Artificial sweat was obtained from Shanghai yuanye Bio-Technology Co., Ltd. poly(3,4-ethylenedioxythiophene)-polystyrenesulfonate (PEDOT:PSS) aqueous solution (Clevios PH1000) with a solid concentration of 1.0–1.3 wt% was purchased from Heraeus (German). Surface active agent (Capstone FS-30) was purchased from DuPont (USA).

Fabrication of GAA FET

After blanket boron doping and photoresist patterning on top of silicon layer, suspended silicon bridge channels were formed using one-step dry etching. Afterwards, SiO_2 and polysilicon were deposited to form a gate-all-around structure. And then traditional lightly-doped drain (LDD) and spacer processes were carried out. Finally, $TiSi_2$ contacts were applied on source/drain regions. The detailed processes and methodologies are covered in our previously published work.[39]

Fabrication of FPCB electrochemical sensors

Before electrochemical modification, carbon ink was first applied to the surface of patterned FPCB electrodes and then heated at 100 °C for 1 hour to dry. Next, Ag/AgCl ink was applied to the reference electrode and also heated at 100 °C for 1 hour to dry. To avoid the potential drift of the reference electrode, a coating solution was prepared by dissolving 79.1 mg PVB and 50 mg NaCl in 1 mL methanol. 0.5 μL of this coating solution was then adopted on the Ag/AgCl electrode. The schematic diagram of the manufacturing process is shown in Fig. S1A.†

To achieve specific detection of Na^+, K^+, and Ca^{2+}, three different types of ion-selective membrane cocktail solutions were prepared and subsequently stored at 4 °C. For the Ca^{2+} selective membrane cocktail solution, 1 mg calcium ionophore II (ETH 129), 33 mg polyvinyl chloride (PVC), 0.55 mg Na-TFPB, and 65.45 mg bis(2-ethylhexyl) sebacate (DOS) were added to 660 μL of tetrahydrofuran (THF). For the K^+ selective membrane cocktail solution, 1 mg valinomycin, 33 mg PVC, 0.55 mg Na-TPB, and 65.45 mg DOS were added to 660 μL of THF. For the Na^+ selective membrane cocktail solution, 1 mg ionophore sodium X, 0.55 mg Na-TFPB, 33 mg PVC, and 130.9 mg DOS were added to 660 μL of THF. For the PEDOT:PSS ink used for ion-selective electrodes, 42.57 μL surface active agent (FS-30), 1.3 mL ethylene glycol (EG) and 20 mL PEDOT:PSS aqueous solution (PH1000) were mixed together, and stirred overnight at 40 °C with a magnetic stirrer. For modifying the ion selective electrodes, 0.5 μL of PEDOT:PSS ink was first drop-casted to the working electrode (extended gate), and then 0.5 μL of ion-selective membrane was drop-casted on the PEDOT:PSS layer, and left at 4 °C overnight.

The enzyme sensing electrodes (for lactate and glucose) were modified using an electrochemical workstation (CHI1000c). First, the electrodes were activated by cyclic voltammetry (CV) in 5 mM L^{-1} sulfuric acid (H_2SO_4, 0–1.5 V, 10 cycles, 50 mV s^{-1}). To enhance sensor sensitivity, gold nanoparticles (AuNPs) were then deposited *via* cyclic voltammetry in a 50 mM/50 mM $HAuCl_4$/HCl solution (−1.4–1 V, 3 cycles, 100 mV s^{-1}). Prussian blue (PB) was then deposited as an intermediate layer on the electrodes using cyclic voltammetry in a solution containing 2.5 mM $FeCl_3$, 100 mM KCl, 2.5 mM $K_3Fe(CN)_6$, and 100 mM HCl (−0.2–0.6 V, 1 cycle for glucose sensors, 14 cycles for lactate sensors, 50 mV s^{-1}). Then, nickel hexacyanoferrate (NiHCF) was deposited (0–0.8 V, 10 cycles, 100 mV s^{-1}) in a solution containing 1 mM $Ni(NO_3)_2$, 0.5 mM $K_3Fe(CN)_6$ and 1 M KCl to prevent the degradation of PB. An enzymatic membrane is prepared by mixing 80 mg ml^{-1} of lactate oxidase/glucose oxidase (in 10 mg ml^{-1} BSA) with a chitosan/multi-walled carbon nanotube (MWCN) solution (1,1 v/v). 1.5 μL of the membrane solution is then drop-casted on the working electrode (extended gate) surface and dried at room temperature. Finally, 1.5 μL of 0.5 wt% Nafion solution is drop-casted on the WE and stored overnight at 4 °C for preparation.

Design and assembly of FPCB electrodes and substrates

The FPCB electrodes and patches were designed using LCEDA Pro and fabricated by JLCPCB. The lactate and glucose sensing electrodes were configured as three-electrode system for modification, while the ion-selective electrodes were designed as two-electrode system. The electrodes were connected to the gold fingers *via* serpentine wires. The substrate of the FPCB was a flexible polyimide (PI), and the GAA FETs were adhered to the pads of the FPCB using conductive silver ink and heated at 150 °C for 0.5 hour. Through gold wire bonding, the source, drain, and gate of the FETs were connected to the corresponding circuit networks. Finally, the electrodes were connected to the FPCB patches by soldered FPCB cables. The process diagram of the GAA FET integration and the patch assembly are shown in Fig. S1B and C.†

Characterization of EGFET flexible sensors

The intrinsic characteristics of GAA FETs and the performance of EGFETs were characterized using FS-Pro

(Primarius, China). The transfer characteristic curves and output characteristic curves of 50 different GAA FETs were tested, and the on/off ratio and subthreshold swing were calculated. The EGFET sensor's performance tests included transfer and output characteristic curves. The threshold voltage was calculated from the transfer characteristic curve ($V_{TH} = V_G^{intercept} - 0.5V_{DS}$, where $V_G^{intercept}$ is the horizontal intercept of the tangent at the point of maximum transconductance, V_{DS} is the voltage between the drain and the source electrode).The FET response was defined as $\Delta V_{TH} = V_{TH}^{marker} - V_{TH0}$, where V_{TH}^{marker} is the threshold voltage at the current concentration, and V_{TH0} is the intrinsic threshold voltage of the device. The limit of detection (LOD) is obtained by subtracting the mean of the blank group from its triple standard deviation (mean − 3σ) and substituting the result into the fitted curve. The bending test of the FPCB electrodes was performed using a stick with the radius of 1.5 cm. The electrodes were bended 800 times in total, and the performance was measured every 200 bending times. The long-term drift test was performed using the commercial artificial sweat and lasted for 6 hours. The performance of the sensors was tested every 1 hour.

Results and discussion

Fig. 1 presents an overview of the EGFET multi-channel measurement sensing patch.§ Fig. 1A illustrates the detection process of the EGFET sensing patch, which enables the detection of lactate, glucose, and various ions.¶ The sensing patch comprises two main parts: a replaceable FPCB sensing electrode array and an FPCB patch containing a GAA FET device array. The sensing electrode array is patterned using FPCB technology, and then carbon electrodes and Ag/AgCl reference electrodes are constructed *via* drop-casting (Fig. S1A and S2†). The radius of the solder mask opening is designed to be 0.1 mm shorter than the radius of the copper pad, making it easy to form patterned carbon electrodes when drop-casting carbon ink (Fig. S3†). The FPCB process is well-suited for the large-scale, cost-effective fabrication of devices, while the PI substrate provides excellent conformability and flexibility for the sensing patch. The 3D gate structure of GAA FETs offers enhanced gate control and provides the sensor with front-end amplification capability. Flexible FPCB electrodes modified *via* electrochemical methods serve as the sensing area for EGFET detection. These modified electrodes enable the selective detection of lactate, glucose, Na^+, K^+, and Ca^{2+}, respectively. Through the FPCB substrate, the sensing electrodes were connected to the GAA FET array.

Specific interactions between the working electrodes and analytes are transduced into electrical signals by the FET, and influencing electrical properties of the FET. Monitoring of target analytes is then achieved by analyzing the effective threshold voltage shifts of the EGFET (Fig. 1B).

Fig. 1C shows an optical image of the EGFET attached to the human body, where a 6 × 6 GAA FET array is integrated onto an FPCB with dimensions of 2.9 mm × 1.4 mm. As shown in Fig. 1D, because of the small area of GAA FETs, it is promising for larger array expansion. Additionally, Fig. 1E presents two optical images of the sensing patch bending in two different directions. With the insulating glue as the encapsulation, the GAA FET and the FPCB substrate were more tightly connected. For validation, bending tests were performed on the FET patch using sticks with different radius (Fig. S4†). Ten bending cycles were performed for each bending radius (0.75–2 cm). The microscopic images of the GAA FETs after bending cycles were shown in Fig. S5.† It can be seen that the cable connection and flexibility of the patch remain nearly unaffected. The threshold voltage (V_{TH}) of the GAA FET was characterized after each bending cycle. From the results in Fig. S6,† the FET performance was almost unaffected, which further demonstrating the potential of the sensor patch for wearable applications.

Characterization of GAA FETs

As the key components, the electrical characteristics of GAA FETs are closely related to the performance of the multi-channel sensing patch. Fig. 2A presents an optical image of GAA FETs tested using a semiconductor parameter analyzer and probe station, along with a magnified schematic of the probe connections.‖ SEM and TEM images of the GAA FETs are shown in Fig. S7.† Fig. S7A and B† illustrate the top view of the GAA FET. Fig. S7C and D† demonstrate the cross section of GAA channel along 1–1′ direction that marked in Fig. S7B.† It can be seen that the suspended silicon channel is completely wrapped by the poly gate. Fig. 2B illustrates the transfer characteristics of GAA FETs under different V_{DS}. Additionally, electrical characterization for 50 randomly selected GAA FETs was conducted (Fig. S8†), showing identical transfer characteristics of these FETs. To further illustrate the homogeneity of the GAA FET, the subthreshold swing (SS) and current on/off ratio were characterized. The SSs of most GAA FETs were in the range of 62–66 mV dec^{-1} (Fig. S9†), with a statistical mean ± standard deviation of 63.97 ± 2.03 mV dec^{-1}. This corresponds to a coefficient of variation (CV) of 3.18%. Furthermore, GAA devices demonstrated excellent SS of about 60 mV dec^{-1} over a wide I_{DS} range (from 10^{-11}–10^{-7} A), with a minimum value of about 60.42 mV dec^{-1} (Fig. S10†). These FETs also showed outstanding on/off ratios of over 10^8 (Fig. S11†). The logarithmic current on/off ratio ($\log_{10}(I_{on}/I_{off})$) shows a mean ± standard deviation of 8.94 ± 0.43 (CV = 4.79%). The statistical characterization of 50 GAA FETs demonstrates the high performance and excellent homogeneity of the devices, which also reflects the robustness of the fabrication process. Fig. 2C shows the output characteristics of the FETs under

§ Some of the artworks were created in BioRender (2025).
¶ https://BioRender.com/w85n515.
‖ https://BioRender.com/x05f219.

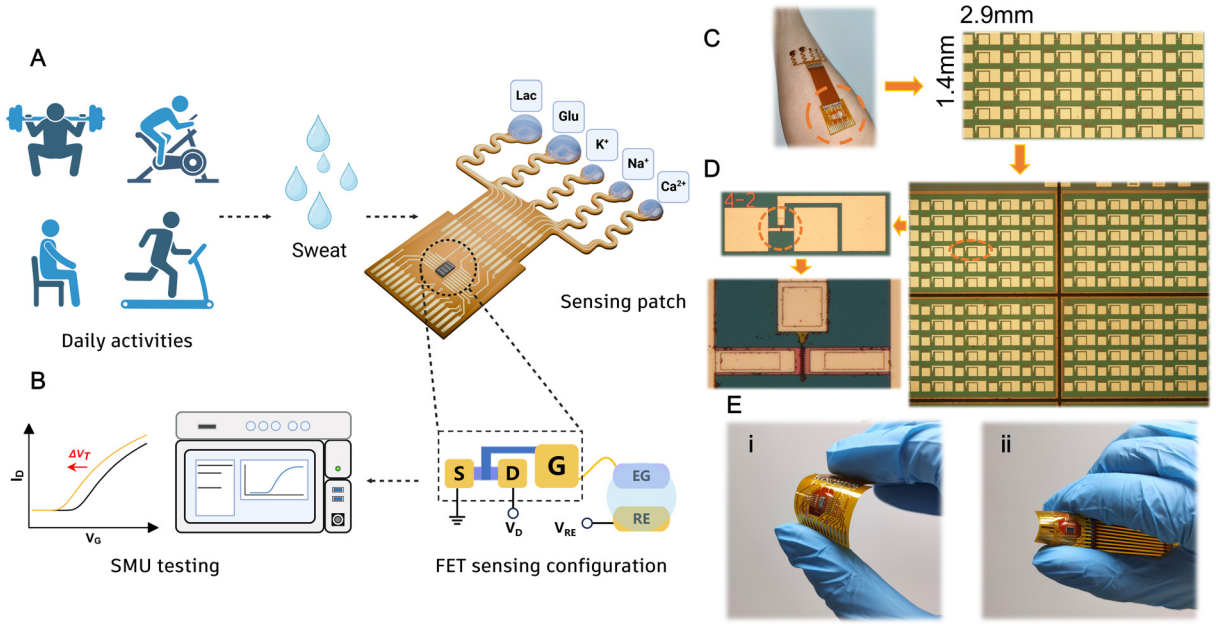

Fig. 1 Schematics and images of the multi-channel EGFET flexible sensing patch. (A) Diagram of muti-channel detection of target analytes. (B) Systematic diagram of the EGFET for sweat detection. (C) Optical image of the EGFET flexible sensing patch on body and microscopic image of the GAAFET array on the FPCB patch. (D) Microscopic image of a larger GAA FET Array and the zoom-in images of the GAA FET structure. (E) The deformation of the FPCB patch integrated with GAA FET under bending in two different directions.

different gate voltages (−0.5 V–1 V with 0.1 V step), demonstrating the evident regulation of current by the gate. Fig. 2D shows the optical image of EGFET sensor measuring, along with a schematic of the probe connection. During solution-based testing, a suitable voltage is applied to the reference electrode (labelled as RE on the FPCB). This voltage is transmitted through the solution to the EG, generating output current. For enzymatic sensors, Prussian blue on the EG undergoes redox reactions with H_2O_2 produced by glucose or lactate oxidation. During this process, the layer of Prussian blue (PB) gains electrons from the EG, altering the gate potential (Fig. 2E). For ion sensors, the specific interaction between ions and the ion-selective membrane (ISM) also causes changes in gate potential (Fig. 2F). Both processes lead to shifts in the EGFETs' effective threshold voltage and output current.

Multiple biomarkers sensing performance of EG-FET

To achieve high sensitivity and selectivity in detecting lactate, glucose, Na^+, K^+, and Ca^{2+}, the FPCB electrodes were electrochemically modified. Fig. 3A demonstrates the process of signal transduction during the measuring of enzyme-based electrodes.** PB on the EG detects the target analytes by measuring the levels of H_2O_2 generated during the aerobic redox reactions of glucose or lactate. In this process, Prussian white (PW), the reduced form of PB, reactions with H_2O_2 and is oxidized to PB. PB then gains electrons from the EG and converts back into PW, allowing the reaction to proceed cyclically. This process induces a change in the potential (φ) at the EG interface. In this process, the reaction of target analytes increases the gate potential and changes the output current of the FET. This demonstrates the feasibility of using EGFETs for the quantitative analysis of lactate or glucose concentrations. According to Kirchhoff's voltage law, the voltage between the FET gate and source (V_{GS}) is a function of the applied reference electrode voltage (V_{ref}) and the junction potential (φ). Consequently, the effective threshold voltage of the EGFET can be expressed as a function of φ.

Based on the regulation of the EG on the gate voltage, the shift in threshold voltage ΔV_{TH} is used to demonstrate the sensor's response to target analytes. Based on the theoretical explanation above, it can be deduced that the concentration of target analytes is negatively correlated with ΔV_{TH}. The performance of two enzyme sensors was characterized in lactate and glucose solutions, respectively. Fig. 3B and D shows the transfer characteristics curves of lactate and glucose at different concentrations. As can be seen, with the increase in analyte concentration, the curves significantly drift in the negative direction of the horizontal axis, confirming the previous hypothesis. The results indicate that ΔV_{TH} is linearly correlated with the logarithm of lactate and glucose concentrations. Specifically, the linearity covers a concentration range of 50–250 μM for glucose detection, with a slope of 107.94 mV dec^{-1} (R^2 = 0.9686, n = 3, Fig. 3C). For lactate detection, the linearity range is 5–20 mM, with a slope of 113.32 mV dec^{-1} (R^2 = 0.9956, n = 3, Fig. 3E). The EG-FET enzyme sensor exhibits a high linear and sensitive response to both lactate and glucose. Furthermore, the output characteristics curves of the EGFET enzyme sensor were measured under conditions of V_{GS} = 0.5 V and V_{GS} = 0.3 V. As

** https://BioRender.com/r84w379.

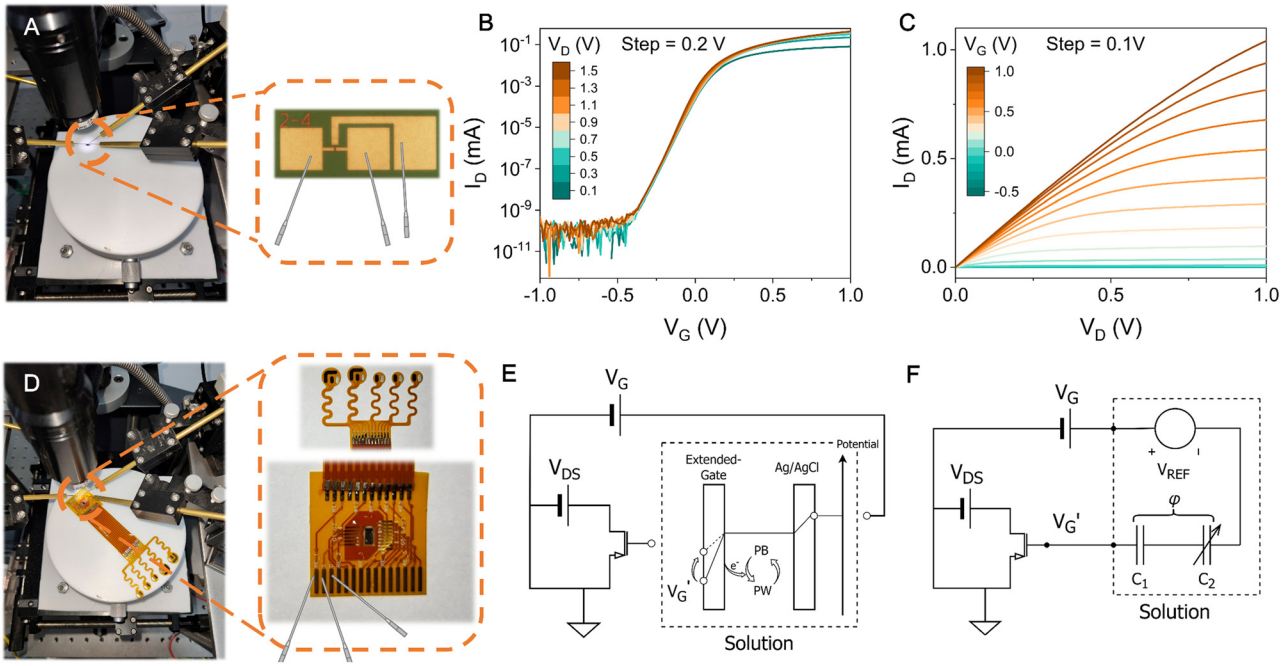

Fig. 2 Intrinsic electrical characterization of GAAFET, along with schematic and principle diagram of the EGFET sensing patch. (A) Photograph of the GAAFET connected to the probe station, along with an enlarged schematic of the pad connection. (B) I_D–V_G curves of GAA FET under different V_D. (C) I_D–V_G curves of GAA FET under different V_G. (D) Photograph of the EGFET sensing patch connected to the probe station, along with an enlarged schematic of the pad connection. (E) Circuit diagram of the EGFET enzyme sensor during detection. (F) Circuit diagram of the EGFET ion sensor during detection.

shown in Fig. S12,† the current I_{DS} between the source and drain increases significantly with the increase in analyte concentration, reflecting the modulation of the gate voltage of the FET. Complete I_D–V_D plots and I_D measurements at other gate voltages are shown in Fig. S13.† For the glucose sensor, I_D–V_D characterization was performed at 0.1 V and 0.5 V, respectively; for the lactate sensor, I_D–V_D characterization was performed at −0.1 V and 0.3 V, respectively, and the output characteristic curves of both showed a significant response to concentration changes.

For ion selective sensors, the same principles used for ISFETs (ion-sensitive field-effect transistors, fabricated with CMOS processes) can be applied for EGFET analysis. This is because the overall structure of EGFETs is similar to ISFETs. The main difference is that the gate of the EGFET is retained and extended to the sensing electrode. Thus, the actual threshold voltage can be expressed as $V_{TH}^{EGFET} = V_{TH}^{FET} + V_{chem}$. Here, V_{chem} is related to the concentration of the ion combined with the ISM, and V_{TH}^{FET} defines the intrinsic threshold voltage of the FET. V_{chem} has a linear relationship with the logarithm of the ion concentration. Fig. 3F shows the measuring process of the EGFET ion sensor.†† Fig. 3G, I and K display the transfer characteristic curves of the EGFET ion sensor, using ΔV_{TH} to characterize the sensor's response. The results exhibit negative logarithmic linear correlation between ΔV_{TH} and ion concentration. Specifically, the linearity covers a concentration range of 5–160 mM for Na^+, with a slope of 104.36 mV dec^{-1} (R^2 = 0.9686, n = 3, Fig. 3H). For K^+ concentrations ranging from 1 to 32 mM, the linear slope is 114.81 mV dec^{-1} (R^2 = 0.9997, n = 3, Fig. 3J). For Ca^{2+} concentrations ranging from 0.25 to 4 mM, the linear slope is 91.69 mV dec^{-1} (R^2 = 0.9989, n = 3, Fig. 3L). The output current I_{DS} of the EGFET under different ion concentrations also demonstrates a significant response (Fig. S12C–E†). Similar to the enzyme sensors, the output current I_{DS} can reach the mA level. Fig. S14† illustrates I_D–V_D curve at other V_G bias. The I_D–V_D characterization was performed at 0.1 V/0.5 V for the sodium and potassium ion sensors, and 0.2 V/0.6 V for the calcium ion sensor. There is a noticeable upward shift in the overall output characteristic curve as V_G becomes larger. Both output characteristic curves showed significant response to concentration. In order to characterize the limit of detection (LOD) and detection range, further detection tests for each biomarker were conducted at lower concentration. The tested range were 5-20 μM for the glucose sensor and 0.1–0.4 mM for the lactate sensor. For the ion sensors, the tested range were 10–10 mM. The results were shown in Fig. S15.† The LODs were 2.45 μM, 31.63 μM, 5.1 μM, 8.3 μM, and 2.68 μM for glucose, lactate, Na^+, K^+ and Ca^{2+}, respectively. Comparison tables (Tables S1–S5†) of recently developed lactate, glucose, Na^+, K^+ and Ca^{2+} sensors are presented in the ESI.† It can be seen that the EGFET sensing patch exhibits advantages in terms of sensitivity, LOD and detection range. Compared to electrochemical sensors, which require both current and voltage measurements, EGFETs can detect concentrations of glucose,

†† https://BioRender.com/v23n071.

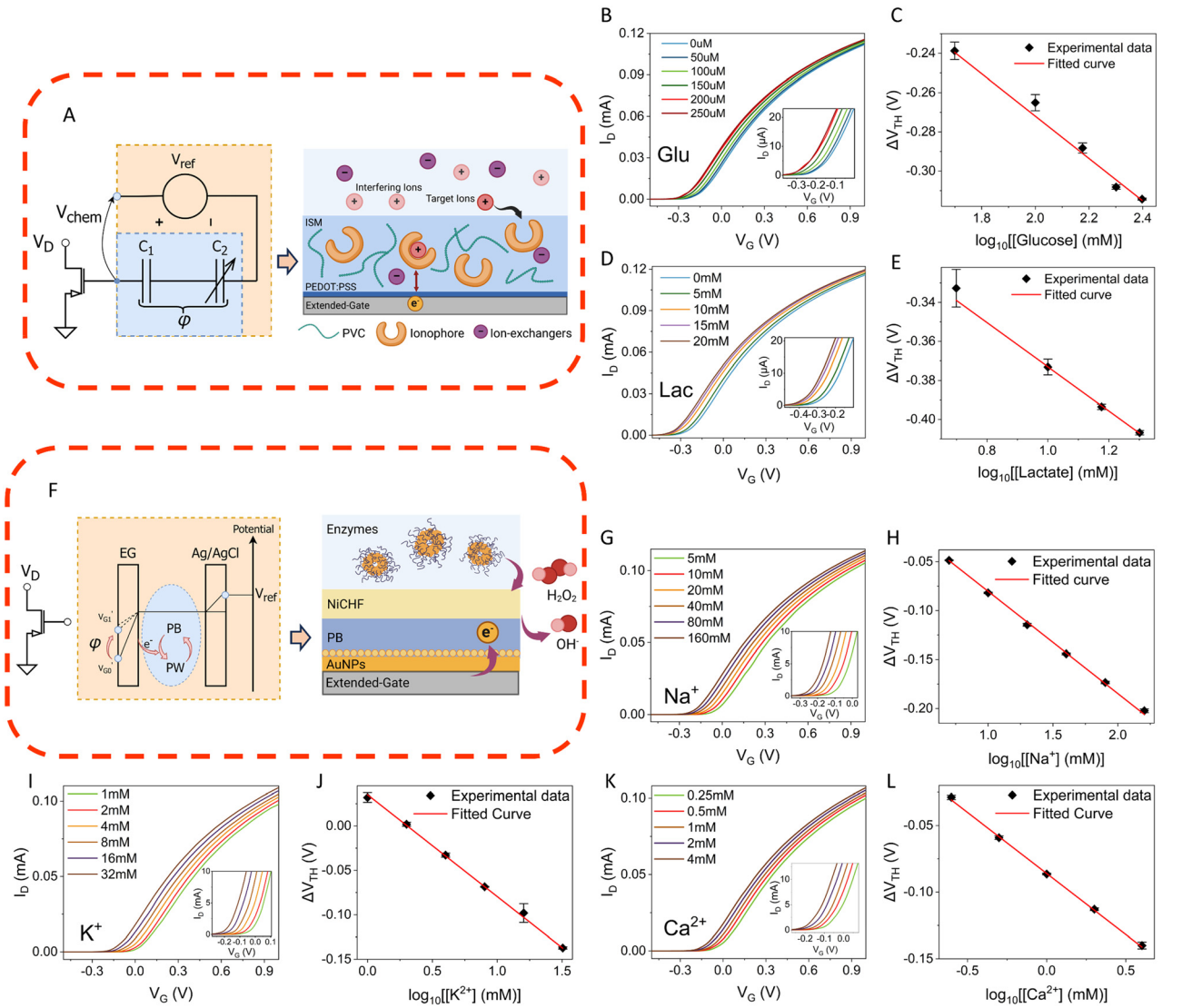

Fig. 3 Characterization of the EGFET enzymatic and ion sensors. (A) Schematic diagram of the reaction on the enzyme sensor (EG) and its effect on the FET gate. PB, Prussian blue. (B) I_D–V_G curves at different glucose concentrations, with the enlarged curve plot (inset) of the initial turn-on phase. (C) Linear fitted curve of ΔV_{TH} *versus* the concentration of glucose. (D) I_D–V_G curves at different lactate concentrations, with the enlarged curve plot (inset) of the initial turn-on phase. (E) Linear fitted curve of ΔV_{TH} *versus* the concentration of lactate. (F) Diagram illustrating the principle of ion-specific binding on the EG electrode surface and its effect on the gate. PEDOT:PSS, poly(3,4-ethylenedioxythiophene) polystyrenesulfonate; ISM, ion-selective membrane; PVC, polyvinyl chloride. I_D–V_G curves and the enlarged curve plots (insets) of the initial turn-on phase at different concentrations of (G) Na^+, (I) K^+ and (K) Ca^{2+}. Linear calibration curve of ΔV_{TH} *versus* the concentration of (H) Na^+, (J) K^+, (L) Ca^{2+}.

lactate and ions by measuring only current response. Thus, this type of sensor patch helps simplify the back-end system design. Besides, the selectivity of the five electrodes was characterised by the addition of different interfering substances to the test solution. The results in Fig. S16† indicated that the EGFET exhibits excellent anti-interference performance. To characterize the stability of the EGFET patch, electrode bending tests as well as long-term drift tests were conducted using artificial sweat. The results (Fig. S17†) indicate that the sensor response remains stable after each bending cycle, and the device response remains consistent after prolonged immersion in sweat(Fig. S18†). To sum up, the EGFET sensing patch has the potential to become an ideal solution for long term health monitoring during normal physiological activities.

Sensing performance in the subthreshold region

The subthreshold region refers to the operating state in which the FET is not fully turned on. In this region, a weak drain current (I_D) exists and the gate voltage is below the threshold voltage (V_{TH}). I_D is exponentially related to V_G in the subthreshold region, indicating that the subthreshold current is extremely sensitive to voltage changes. According to Fig. S10,† the GAAFET exhibits excellent subthreshold current response characteristics due to its unique structure:

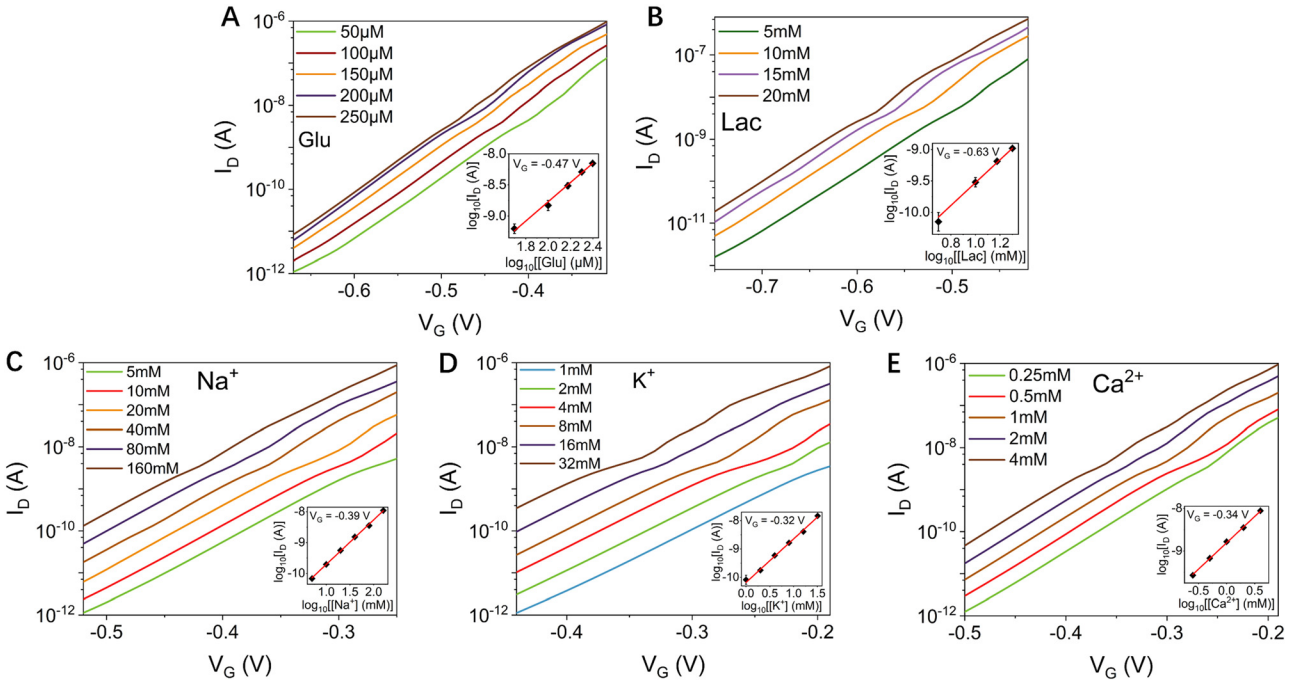

Fig. 4 Characterization of the sensing performance in the subthreshold region. (A) I_D–V_G curves in the subthreshold region and linear fitted curve (inset) for glucose. (B) I_D–V_G curves in the subthreshold region and linear fitted curve (inset) for lactate. (C) I_D–V_G curves in the subthreshold region and linear fitted curve (inset) for Na^+. (D) I_D–V_G curves in the subthreshold region and linear fitted curve (inset) for K^+. (E) I_D–V_G curves in the subthreshold region and linear fitted curve (inset) for Ca^{2+}.

the subthreshold swing (SS) remains stable and small when I_D is less than 10^{-8}A. The small SS makes the I_D highly sensitive to V_G changes, which can improve the detection sensitivity of the sensor.

In this section, the subthreshold region of the transfer characteristic curve is selected for analysis, and the current response for different analyte concentrations was linearly fitted. As shown in Fig. 4A and 5E, the subthreshold current responses of various analytes indicates that the logarithmic value of the current ($\log_{10}I_D$) was linearly related to the logarithmic value of the concentration ($\log_{10}C$). For Na^+ sensor, the fitted linear regression equation is $\log_{10}I_D = -11.15223 + 1.44478 \times \log_{10}C_{[Na^+]}$. For K^+ sensor, the fitted linear regression equation is $\log_{10}I_D = -10.1747 + 1.53042 \times \log_{10}C_{[K^+]}$. For Ca^{2+} sensor, the fitted linear regression equation is $\log_{10}I_D = -8.80663 + 1.23348 \times \log_{10}C_{[Ca^{2+}]}$. For glucose sensor, the fitted linear regression equation is $\log_{10}I_D = -11.87127 + 1.55047 \times \log_{10}C_{[glu]}$. For lactate sensor, the fitted linear regression equation is $\log_{10}I_D = -11.34805 + 1.82127 \times \log_{10}C_{[lac]}$. In order to clearly demonstrate the unique properties of the response in the subthreshold region, the currents were normalised. A set of current values from the linear region were also selected and normalised. The comparisons in Fig. S19† demonstrate that for each analyte, the normalized currents in the subthreshold region (I_{Dsub}) were much larger than the normalized current in the linear region ($I_{Dlinear}$). Table. S6† shows that I_{Dsub}:$I_{Dlinear}$ can be as large as 80.63. This result shows that the response in the subthreshold region is more sensitive.

In vitro sweat analysis using EG-FET

To validate the performance of the EGFET sensor in detecting human sweat, the researchers recruited three volunteers to collect sweat from their foreheads during sauna, weight lifting and cycling, respectively. For the sauna volunteer, 5-minute breaks were taken every 10 minutes, with sweat samples collected every 15 minutes. For the weight-lifting volunteer, 5-minute breaks were taken every 15 minutes, and sweat samples were collected every 20 minutes. For the cycling volunteer, the first part of cycling began with high intensity and the intensity gradually decreased, followed by the second part of cycling at a steady moderate intensity. During this process, sweat samples were collected every 15 to 30 minutes. Fig. 5 shows the dynamic changes of five biomarkers over time.‡‡ Since ΔV_{TH} is negatively correlated with biomarker concentrations, the vertical axis was inverted. As shown in Fig. 5A, the glucose and lactate levels of the volunteers' sweat fluctuated slightly during sauna, while the ion concentrations decreased slowly. This suggests that electrolyte loss continued when the body was sweating heavily at high temperatures. The changes in biomarkers during weight-lifting was similar to the changes during cycling. Glucose concentration first rose and then fell, and finally rose to a steady level, whereas lactate concentrations first increased and then decreased to a steady level. Ion concentrations showed an overall decreasing trend. These results suggests that there might be a large amount of

‡‡ https://BioRender.com/f17f971.

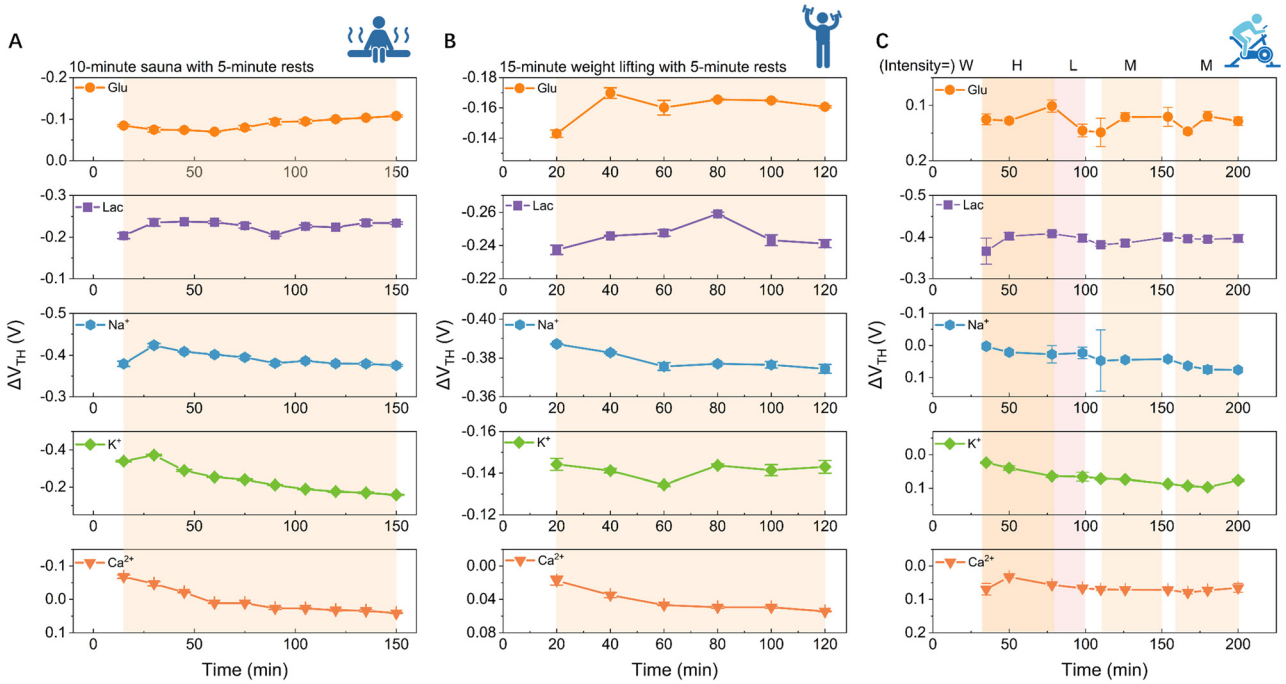

Fig. 5 Characterization of the EGFET sensing patch using sweat collected during three different physical activities: (A) sauna, (B) weight lifting and (C) cycling. For the results of cycling, W = warm up, H = high intensity, L = low intensity, and M = moderate intensity.

glycogenolysis and blood lactate accumulation at the beginning or at higher intensity. As the exercise continued and intensity decreased, the glucose level decreased and then slightly increased under hormonal regulation. At the same time, lactate began to be removed from muscle and other tissues (lactate cycle) and the lactate level gradually remained stable. Besides, a steady decline in ion concentrations suggest a gradual loss of electrolytes with heavy sweating during exercise. The sweat tests demonstrated that the EGFET sensing patch could to some extent reflect the physiological state of the human body.

Conclusions

In this work, the proposed flexible EGFET sensor array patch, combines gate-all-around field-effect transistors (GAA FETs) and FPCB patches to provide a promising solution for wearable sweat monitoring applications. This innovative sensing patch enables large-scale, low-cost manufacturing and flexible integration. It effectively addresses the limitations of traditional FET sensors and electrochemical sensors. The GAA FETs provide high transconductance, low driving voltage and better electron mobility, thereby enhances the sensing capability. The characterisation of the response in the subthreshold region suggests that the GAA FET-based sensor holds promise for more sensitive detection than conventional FET sensors. The systematic characterization of this patch demonstrated its excellent performance in detecting multiple biomarkers such as glucose, lactate, Na^+, K^+, and Ca^{2+}, which are essential for understanding overall health information. The patch is highly expandable. By connecting extended gates with different functions, it is possible to achieve the detection of a wide range of biomarkers. By replacing the extended gates with physical signal transducers (strain, pressure, temperature, *etc.*), it can enable sensitive detection of physical signals to provide more comprehensive personal health information. Additionally, the FPCB substrate of the patch makes it easy to integrate signal processing and wireless data transmission units. This work not only provides a novel approach to development of advanced multi-channel wearable sensors, but also paves the way for comprehensive physiological monitoring and health status assessment, and is promising to bring about a change in the development of wearable sensing technologies. In the future, our research will focus on the development of wearable multimodal EGFET sensing system to collect biochemical and physical health information. Our goal also includes integrating artificial intelligence for data processing to provide individual health profiles.

Data availability

The authors confirm that the data supporting the findings of this study are available within the article and as its ESI.†

Author contributions

Z. Xing: methodology, visualization, writing – original draft, conceptualization. Q. Liu: methodology, visualization, conceptualization. B. Lin: methodology, investigation. S. Li: visualization. Y. Liu: investigation. G. Zhang: methodology, visualization. W. Yu: methodology. Z. Wu: methodology and supervision, project administration, writing – review & editing. H. Mao: project administration, funding acquisition, writing –

review & editing. All authors have given approval to the final version of the manuscript.

Conflicts of interest

There are no conflicts to declare.

Acknowledgements

This research was funded by the National Key R&D Program of China (grant no. 2022YFF1202700), Program of Science and Technology Commission of Shanghai Municipality (grant no. 23141901100), the National Natural Science Foundation of China (grant no. 62231025), Shanghai Municipal Science and Technology Major Project (grant no. ZD2021CY001), Science and Technology Program of Guangzhou (grant no. 2024B03J0022), Shenzhen Longgang District Medical and Health Technology Key Support Project (grant no. LGKCYLWS2024-12), Science and Technology Project of Haihe Laboratory of Modern Chinese Medicine(grant no. 22HHZYSS00011), and Shanghai Engineer &Technology Research Center of Internet of Things for Respiratory Medicine (grant no. 20DZ2254400).

Notes and references

1 B. Zhong, X. Qin, H. Xu, L. Liu, L. Li, Z. Li, L. Cao, Z. Lou, J. A. Jackman, N.-J. Cho and L. Wang, *Nat. Commun.*, 2024, **15**, 624.
2 B. Lin, F. Li, J. Hui, Z. Xing, J. Fu, S. Li, H. Shi, C. Liu, H. Mao and Z. Wu, *ACS Sens.*, 2025, **10**, 225–235.
3 A. Childs, B. Mayol, J. Lasalde-Ramirez, Y. Song, J. R. Sempionatto and W. Gao, *ACS Nano*, 2024, **18**, 24605–24616.
4 Y. Sun, J. Wang, Q. Lu, T. Fang, S. Wang, C. Yang, Y. Lin, Q. Wang, Y. Lu and D. Kong, *ACS Nano*, 2024, **18**, 2335–2345.
5 H. Zhao, X. Zhang, Y. Qin, Y. Xia, X. Xu, X. Sun, D. Yu, S. M. Mugo, D. Wang and Q. Zhang, *Adv. Funct. Mater.*, 2023, **33**, 2212083.
6 K. Mahato, T. Saha, S. Ding, S. S. Sandhu, A.-Y. Chang and J. Wang, *Nat. Electron*, 2024, **7**, 735–750.
7 T. Sun, J. Hui, L. Zhou, B. Lin, H. Sun, Y. Bai, J. Zhao and H. Mao, *Sens. Actuators, B*, 2022, **368**, 132184.
8 H. Y. Y. Nyein, W. Gao, Z. Shahpar, S. Emaminejad, S. Challa, K. Chen, H. M. Fahad, L.-C. Tai, H. Ota, R. W. Davis and A. Javey, *ACS Nano*, 2016, **10**, 7216–7224.
9 Z. Xing, J. Hui, B. Lin, Z. Wu and H. Mao, *Chemosensors*, 2023, **11**, 470.
10 X. Xuan, C. Chen, A. Molinero-Fernandez, E. Ekelund, D. Cardinale, M. Swarén, L. Wedholm, M. Cuartero and G. A. Crespo, *ACS Sens.*, 2023, **8**, 2401–2409.
11 M. Mansour, M. Saeed Darweesh and A. Soltan, *Alexandria Eng. J.*, 2024, **89**, 224–243.
12 T. Sun, J. Hui, B. Lin, H. Sun, L. Zhou, J. Zhao and H. Mao, *Appl. Mater. Today*, 2023, **34**, 101910.
13 S. Emaminejad, W. Gao, E. Wu, Z. A. Davies, H. Yin Yin Nyein, S. Challa, S. P. Ryan, H. M. Fahad, K. Chen, Z. Shahpar, S. Talebi, C. Milla, A. Javey and R. W. Davis, *Proc. Natl. Acad. Sci. U. S. A.*, 2017, **114**, 4625–4630.
14 B. Lin, T. Sun, J. Hui, L. Zhou, Z. Xing, Z. Wu and H. Mao, *ACS Sens.*, 2024, **9**, 1272–1279.
15 B. K. Sarker, R. Shrestha, K. M. Singh, J. Lombardi, R. An, A. Islam and L. F. Drummy, *ACS Nano*, 2023, **17**, 20968–20978.
16 B. Wang, C. Zhao, Z. Wang, K.-A. Yang, X. Cheng, W. Liu, W. Yu, S. Lin, Y. Zhao, K. M. Cheung, H. Lin, H. Hojaiji, P. S. Weiss, M. N. Stojanović, A. J. Tomiyama, A. M. Andrews and S. Emaminejad, *Sci. Adv.*, 2022, **8**, eabk0967.
17 Y. Zhang, D. Chen, W. He, N. Chen, L. Zhou, L. Yu, Y. Yang and Q. Yuan, *Adv. Mater.*, 2023, 2306252.
18 M. T. Hwang, M. Heiranian, Y. Kim, S. You, J. Leem, A. Taqieddin, V. Faramarzi, Y. Jing, I. Park, A. M. van der Zande, S. Nam, N. R. Aluru and R. Bashir, *Nat. Commun.*, 2020, **11**, 1543.
19 J. Song, H. Liu, Z. Zhao, P. Lin and F. Yan, *Adv. Mater.*, 2024, **36**, 2300034.
20 J. Ouyang, Y. Li, F. Yang, X. Wu, Z. Qiu and J. Shu, *Adv. Funct. Mater.*, 2024, **34**, 2405212.
21 Y. Jin Na, J. Park, S.-C. Park, W. Gyun Park, K.-W. Kim, B. Wang and J.-H. Ahn, *IEEE Sens. J.*, 2024, **24**, 25275–25283.
22 H.-J. Jang, T. Lee, J. Song, L. Russell, H. Li, J. Dailey, P. C. Searson and H. E. Katz, *ACS Appl. Mater. Interfaces*, 2018, **10**, 16233–16237.
23 M.-Z. Li, S.-T. Han and Y. Zhou, *Adv. Intell. Syst.*, 2020, **2**, 2000113.
24 Q. Peng, Q. Zeng, F. Wang, X. Wu, R. Zhang, G. Shi and M. Zhang, *ACS Nano*, 2023, **17**, 21984–21992.
25 X. Chen, Y. Liang, N. Tang, C. Li, Y. Zhang, F. Xu, G. Shi and M. Zhang, *Biosens. Bioelectron.*, 2024, **249**, 116016.
26 G. P. Kuppuswamy, M. S. Shabanur Matada, G. Marappan, M. Y. Mulla, S. Velappa Jayaraman, C. Di Natale and Y. Sivalingam, *ACS Appl. Electron. Mater.*, 2023, **5**, 3268–3279.
27 H.-Y. Ho, W.-S. Kao, P. Deval, C.-Y. Dai, Y.-H. Chen, M.-L. Yu, C.-H. Lin and L.-S. Yu, *Sens. Actuators, B*, 2023, **394**, 134278.
28 L. Shi, L. Gong, Y. Wang, Y. Li and Y. Zhang, *Sens. Actuators, B*, 2024, **400**, 134944.
29 Y. Zheng, R. Omar, R. Zhang, N. Tang, M. Khatib, Q. Xu, Y. Milyutin, W. Saliba, Y. Y. Broza, W. Wu, M. Yuan and H. Haick, *Adv. Mater.*, 2022, **34**, 2108607.
30 T. Mano, K. Nagamine, Y. Ichimura, R. Shiwaku, H. Furusawa, H. Matsui, D. Kumaki and S. Tokito, *ChemElectroChem*, 2018, **5**, 3881–3886.
31 H. Richardson, B. Thompson, K. Peterson, T. Songkakul, K. Sode, M. Daniele, A. Bozkurt and S. Pavlidis, in *2024 46th Annual International Conference of the IEEE Engineering in Medicine and Biology Society (EMBC)*, 2024, pp. 1–4.
32 C. Shen, X. Xi, D. Wu, X. Guo, Y. Su and R. Liu, *Biosens. Bioelectron.*, 2025, **267**, 116787.
33 S. Sheibani, L. Capua, S. Kamaei, S. S. A. Akbari, J. Zhang, H. Guerin and A. M. Ionescu, *Commun. Mater.*, 2021, **2**, 1–10.
34 R. Omar, M. Yuan, J. Wang, M. Sublaban, W. Saliba, Y. Zheng and H. Haick, *Sens. Actuators, B*, 2024, **398**, 134788.
35 D. Probst, J. Twiddy, M. Hatada, S. Pavlidis, M. Daniele and K. Sode, *Anal. Chem.*, 2024, **96**, 4076–4085.

36 C. Huang, D. Li, J. Liu, S. Hou, W. Yang, H. Wang, J. Wang, Z. Wang, F. Li, Z. Hao, S. Huang, X. Zhao, P. Hu and Y. Pan, *Adv. Funct. Mater.*, 2023, 2309447.
37 Q. Liu, Z. Mu, C. Liu, L. Zhao, L. Chen, Y. Yang, X. Wei and W. Yu, *IEEE Electron Device Lett.*, 2021, **42**, 657–660.
38 L. Qin, C. Li, Y. Wei, G. Hu, J. Chen, Y. Li, C. Du, Z. Xu, X. Wang and J. He, *IEEE Access*, 2023, **11**, 14028–14042.
39 Q. Liu, Z. Mu, C. Liu, L. Zhao, L. Chen, Y. Yang, X. Wei and W. Yu, *IEEE Electron Device Lett.*, 2021, **42**, 657–660.